PCCP

COMMUNICATION

View Article Online
View Journal

Engineering self-assembled N-doped graphene–carbon nanotube composites towards efficient oxygen reduction electrocatalysts†

Cite this: DOI: 10.1039/c4cp00757c

Received 21st February 2014,
Accepted 3rd April 2014

DOI: 10.1039/c4cp00757c

www.rsc.org/pccp

Yun Zhang,[ab] Wen-Jie Jiang,[ab] Xing Zhang,[b] Lin Guo,[ab] Jin-Song Hu,*[b] Zidong Wei*[a] and Li-Jun Wan[b]

The importance of the oxygen reduction reaction (ORR) in fuel cells and high energy density metal–air batteries has attracted intense research interests in looking for low-cost ORR catalysts as substitutes for expensive and scarce Pt-based catalysts. N-doped graphene and carbon nanotubes prepared in a low-cost and scalable way have demonstrated their potential although the performance still needs to be improved. In view of the requirements for a high-performance ORR electrocatalyst, this work focused on developing the nanocomposites of N-doped reduced graphene oxide (N-rGO) and N-doped carbon nanotubes (N-CNT) as low-cost efficient ORR catalysts by integrating the advantages of abundant highly-active sites from N-rGO and a three-dimensional conductive network for efficient mass and electron transport from N-CNT. By optimizing the preparation method and dedicatedly tuning the composition, the much enhanced ORR activity and superior durability and tolerance to methanol were achieved for the self-assembled N-doped composite (N-rGO–CNT) at a mass ratio of 1 : 5 rGO/CNT. Further improvement of the ORR electrocatalytic activity of the composite was also demonstrated by introducing iron into the composite.

Introduction

Designing low-cost high-performance electrocatalysts for an efficient oxygen reduction reaction (ORR) is very important in a range of energy applications including fuel cells, metal–air batteries and chlor-alkali electrolysis.[1–3] However, the further development and large-scale application of these technologies hampered by the sluggish kinetics of ORR stemmed from the difficulty in breaking the strong O=O bond, as well as the issues of the state-of-the-art Pt-based catalysts such as high cost, short supply, poor durability, and insufficient tolerance to fuel crossover.[4] Therefore, enormous efforts have been devoted towards investigating low-cost substitutes for commercial Pt/C catalysts, including metal–nitrogen complexes on carbon supports,[5] transition metal chalcogenide,[6] oxide,[7] and nitride,[8] heteroatom-doped carbon materials,[9–12] and their combinations.[13–17]

Graphene, as an ultrathin two-dimensional honeycomb network of sp^2-hybridized carbon, displays many distinct properties required for a good electrocatalyst, including high surface area, good electrical conductivity and excellent mechanical properties. N,[10,18,19] P,[12,20] S[10,21] and B[19,20] doped as well as dual-doped and trinary-doped graphene have attracted much attention to explore its potential as an ORR electrocatalyst since heteroatom doping could provide abundant highly-active catalytic sites. Although tremendous work has been done, the development of heteroatom doped graphene with high activity for catalyzing ORR is still challenging. Heteroatom doped graphene (usually referred to as reduced graphene oxide, rGO) catalysts have two main issues. The first one is incomplete reduction for graphene made by low-cost chemical oxidation and an exfoliation method, which severely deteriorates its performance.[22] The second one is that the stacking of graphene sheets causes the substantial amount of catalytic sites inaccessible for O_2 and ions, and thus depresses the efficiency of the catalytic reaction.[23,24]

Taking into account the advantages and issues of graphene as an electrocatalyst, one-dimensional carbon nanotubes (CNT) could be introduced into graphene materials as a highly conductive three-dimensional (3D) network to construct 3D graphene–CNT composite materials.[25] These materials have been successfully used in solar cells and energy storage devices.[22,26–28] For ORR application, the incorporation of CNT can not only solve the mass transfer issue caused by the stacking and agglomeration in graphene-based catalysts, but also greatly enhance the electron transport through building a 3D interpenetrating conductive network and the close electron coupling between graphene and CNT. Although some methods have been developed to synthesize graphene–CNT

[a] State Key Laboratory of Power Transmission Equipment & System Security and New Technology, College of Chemistry and Chemical Engineering, Chongqing University, Chongqing 400044, China. E-mail: zdwei@cqu.edu.cn
[b] Beijing National Laboratory for Molecular Sciences, Key Laboratory of Molecular Nanostructure and Nanotechnology, Institute of Chemistry, Chinese Academy of Science, 2 North 1st Street, Zhongguancun, Beijing 100190, China. E-mail: hujs@iccas.ac.cn

† Electronic supplementary information (ESI) available. See DOI: 10.1039/c4cp00757c

composites[24,29,30] and initial efforts to use graphene–CNT for catalyzing ORR have been attempted,[24,30] no reports have focused on investigating the influence of its preparation method and composition on the performance; and the catalytic performance for ORR of the reported composites still needs to be improved.[22,27]

Herein, we developed a facile solution self-assembly method to prepare the composites of rGO, CNT and a nitrogen-rich source, followed by heat treatment to achieve N-doped rGO–CNT composites (N-rGO–CNT). By taking advantage of the abundant highly-active sites from N-doped rGO and the three-dimensional conductive network for efficient mass and electron transport from N-doped CNT, the composites of N-rGO–CNT demonstrated their potential as low-cost efficient ORR catalysts. More importantly, by dedicatedly engineering the composition of N-rGO–CNT, it was found that the mass ratio of rGO and CNT in the composite significantly affects the electrocatalytic activity of the composite for ORR. The highest ORR activity was achieved when the mass ratio of rGO and CNT in the composite was 1 : 5, regardless of the preparation method for obtaining the composite. As a result, an N-rGO–CNT composite ORR catalyst with a much enhanced ORR activity and superior durability and tolerance to methanol was obtained. The catalytic performance of the composite can be further improved by simply introducing an iron source into N-rGO–CNT during thermal treatment.

Results and discussion

rGO–CNT composites were prepared *via* a simple solution self-assembly process. In a typical synthesis, CNT (40 mg) and melamine (240 mg) were dispersed into a DMF solution (240 mL) by sonicating the mixture for an hour. The graphene oxide (GO) solution (3.08 mL, 2.60 mg mL^{-1}) pre-prepared by the modified Hummers method was then added into the mixture, followed by sonication for another hour. The mass ratio of rGO and CNT in this case was 1 : 5. After stirring at room temperature overnight, the solution mixture was dried by rotary evaporation at 85 °C. Nitrogen doping was achieved by heat treating the dried mixture at 900 °C for an hour under an Ar atmosphere.

The morphologies of the synthesized N-rGO–CNT composites were first investigated by scanning electron microscopy (SEM) and transmission electron microscopy (TEM). Fig. 1 displays the representative SEM and TEM images of the sample. From the SEM images (Fig. 1a and b), it is distinctly observed that CNT and graphene sheets combined together and were in close contact. In TEM visualization, no obvious CNT bundles or graphene agglomerates were observed. The typical TEM image shown in Fig. 1c clearly confirms the co-existence of CNT and graphene layers. The very thin layers and wrinkled folds are typical features of graphene layers. The tubular nanostructures with an average diameter of around 50 nm are CNT unarguably. It is also seen that some graphene layers wrapped CNT, indicating that CNT and graphene layers were well linked together.

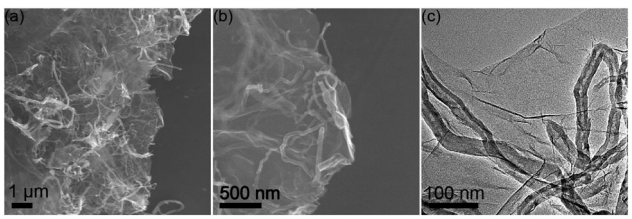

Fig. 1 (a), (b) SEM and (c) TEM images of N-rGO–CNT.

Since the catalytic performance of the N-rGO–CNT composite was supposed to be the result of balancing the advantages of N-rGO and N-CNT, the composition of graphene and CNT in the N-rGO–CNT composite would probably affect its electrocatalytic activity for ORR. In order to investigate this effect, six samples with different mass ratios of GO to CNT (0/10, 1/10, 2/10, 6/10, 10/10, and 10/0) were prepared in this study by only adjusting the amount of GO solution and melamine and keeping the amount of CNT and the content of melamine in the composite constant. These samples were denoted N-CNT, N-rGO–CNT-0.1, N-rGO–CNT-0.2, N-rGO–CNT-0.6, N-rGO–CNT-1, and N-rGO, respectively.

The electrocatalytic performances of all N-rGO–CNT composites were first evaluated by linear sweep voltammetry (LSV). The measurements were implemented on a rotating disk electrode (RDE) with a constant catalyst loading of 600 μg cm^{-2} in 0.1 M O_2-saturated KOH solution at a rotation rate of 1600 rpm. As seen in Fig. 2a, the electrocatalytic activities of the composites are strongly dependent on the mass ratio of rGO and CNT in composites. The on-set potential of pure N-rGO for ORR is more positive than that of other catalysts, suggesting that it has more active catalytic sites. However, its LSV curve does not show obvious diffusion-limited current density and the current density at low potential is the

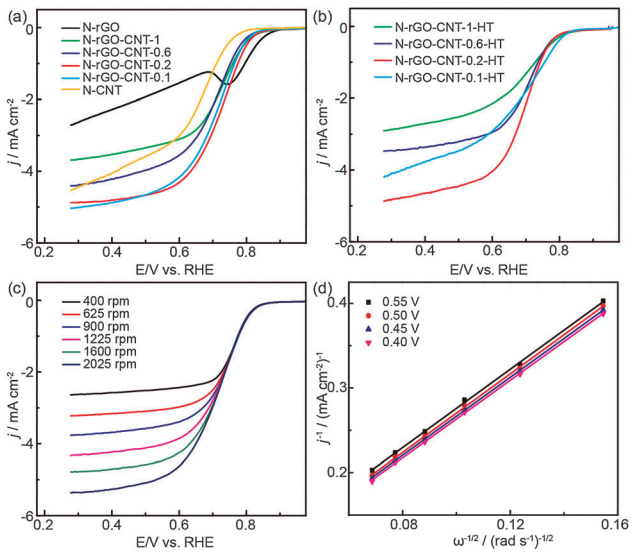

Fig. 2 (a) LSV curves of N-rGO–CNTs with different compositions prepared by a solution self-assembly route. (b) LSV curves of N-rGO–CNTs with different compositions prepared by a hydrothermal method. In both (a) and (b), all curves recorded in 0.1 M O_2-saturated KOH at a scan rate of 10 mV s^{-1} and a rotation speed of 1600 rpm. (c) Polarization curves of N-rGO–CNT-0.2 recorded in 0.1 M O_2-saturated KOH at a scan rate of 10 mV s^{-1} and different rotation speeds. (d) Koutecky–Levich plots at 0.40 V, 0.45 V, 0.50 V and 0.55 V *vs.* RHE calculated from RDE tests at various rotating speeds.

lowest in all samples, which indicates that it undergoes severe mass transfer. This can be corroborated by the fact that the LSV curves of N-rGOs tend to be normal when the catalyst loading was decreased to 150 μg cm^{-2}, although the on-set potential correspondingly decreases as well at lower catalyst loading (see Fig. S1 in ESI†). Moreover, pure N-CNT shows the most negative on-set potential and half-wave potential ($E_{1/2}$), indicating its inferior performance in catalyzing ORR. However, it is interestingly noted that the ORR electrocatalytic activity of the materials is prominently enhanced by combining small amounts of N-rGO into N-CNT. For example, upon addition of 10% rGO (*vs.* CNT), the $E_{1/2}$ and on-set potential of the composite catalyst were dramatically positively shifted compared to pure N-CNT. The current density at −0.48 V (*vs.* RHE) of the composite increased to 4.72 from 2.02 for N-rGO and 3.68 mA cm^{-2} for N-CNT. The best performance was further achieved at a mass ratio of rGO and CNT of 1 : 5. The $E_{1/2}$ of the composite N-rGO–CNT-0.2 is 98 mV positive than that of N-CNT. Further addition more rGO resulted in the decrease in the ORR activity in terms of a negative shift of $E_{1/2}$ and on-set potential as well as the decreased current density. Furthermore, this dependency of catalytic performance on the relative content of rGO and CNT was found in the rGO–CNT composites prepared by other methods. Besides the solution self-assembly method which was used to prepare above-mentioned composites, we also prepared rGO–CNT composites *via* a hydrothermal route according to the literature[24] and measured the catalytic performance of N-doped rGO–CNT for ORR. As shown in Fig. 2b, the composites prepared at a mass ratio of rGO and CNT of 1 : 5 also demonstrate the best performance in catalyzing ORR. These facts indicate that the electrocatalytic performance of the N-doped rGO–CNT composites for ORR should be the result of balancing mass transfer and the amount of catalytically active sites.

In order to further evaluate the performance of the present N-rGO–CNT composite catalysts, a series of LSV experiments were carried out on RDE loaded with a N-rGO–CNT-0.2 catalyst at different rotating speeds from 400 rpm to 2025 rpm in 0.1 M O_2-saturated KOH solution. As shown in Fig. 2c, the limited current density increases with increase in the rotation rate of RDE. The Koutecky–Levich (K–L) plots at several potentials were calculated *via* the K–L equation to give insight into the electron transfer process during ORR (see ESI† for details). It is clearly seen from Fig. 2d that all K–L plots at different potentials are nearly parallel. The number of electron transfer calculated from the slopes of K–L plots is around 3.9 for all four plots, which suggests that the highly efficient and beneficial four electron reduction pathway dominates in ORR when N-rGO–CNT-0.2 was used as the catalyst.

It was reported that nitrogen species in N-doped carbon materials played an important role in enhancing the ORR catalytic performance of catalysts and was considered as the catalytically active sites. The nitrogen content and chemical bonding state would affect the activity of catalysts.[31–35] Therefore, it is necessary to analyse the nitrogen content and chemical states in current catalysts for understanding the difference in their ORR catalytic activities. Fig. 3 shows the typical results of X-ray photoelectron spectroscopy (XPS) measurements. As shown in Fig. 3a, the

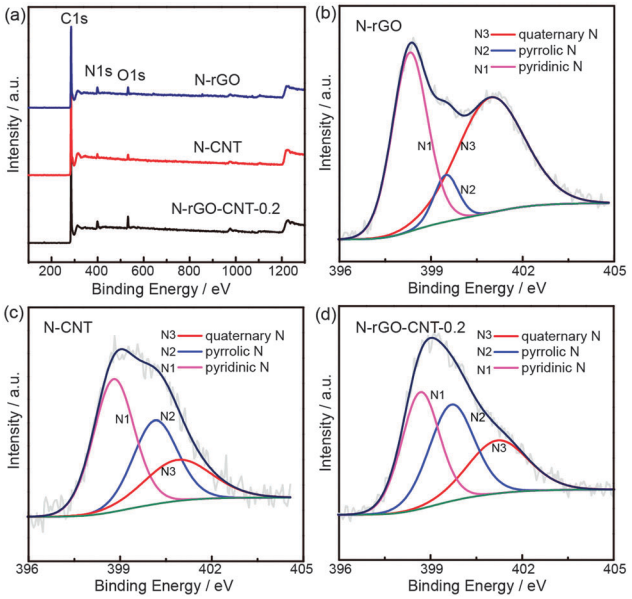

Fig. 3 (a) Wide-scan survey XPS spectra of N-rGO, N-CNT and N-rGO–CNT-0.2. (b–d) High-resolution N 1s signals in XPS spectra of N-rGO, N-CNT and N-rGO–CNT-0.2, respectively.

survey scans recorded on N-rGO, N-CNT and N-rGO–CNT-0.2 display obvious nitrogen signals, affirming the successful introduction of nitrogen in all samples. The intensities of nitrogen signals in the three curves are different. Quantitative analysis presented in Table 1 reveals that the nitrogen content in N-rGO reached up to 6.68 at%, which could be attributed to the abundant defect sites in GO. In contrast, only 2.05 at% nitrogen was introduced into N-CNT. After introducing 20% rGO, the nitrogen content in the N-rGO–CNT-0.2 composite increased to 5.02 at%, suggesting that the introduction of rGO can significantly promote the amount of catalytically active sites. On the other hand, the bonding states of nitrogen in three materials were further investigated by deconvoluting high-resolution N 1s signals into the components corresponding to pyridinic type, pyrrolic type, and quaternary type nitrogen (Fig. 3b–d). The selected binding energy for each type of N and the quantitative analysis are summarized in Table S1 (see ESI†) and Table 1. It can be seen that the fractions of each type of nitrogen are different in the three samples. The pyridinic and quaternary type N dominated in N-rGO, which were reported to

Table 1 Nitrogen contents and analysis based on XPS spectra

Sample	N[a]	N1[b]	N2[c]	N3[d]
N-rGO	6.68	41.92	7.58	50.50
N-CNT	2.05	45.46	31.36	23.18
N-rGO–CNT-0.2	5.02	36.90	36.53	26.57

[a] Total nitrogen content (at%). [b] Fraction (%) of pyridinic-N (N1), calculated from deconvoluted high-resolution N 1s spectra. [c] Fraction (%) of pyrrolic-N (N2), calculated from deconvoluted high-resolution N 1s spectra. [d] Fraction (%) of quaternary-N (N3), calculated from deconvoluted high-resolution N 1s spectra.

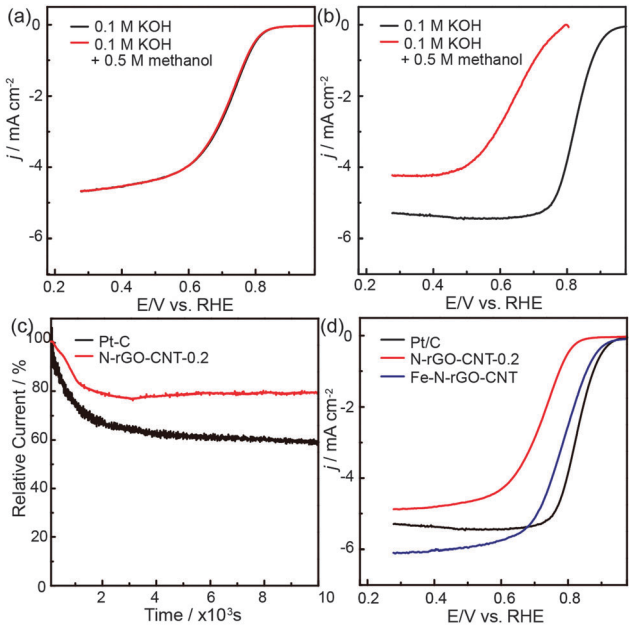

Fig. 4 RDE polarization curves of (a) N-rGO–CNT-0.2 and (b) commercial Pt/C in the presence or absence of 0.5 M methanol. (c) Current–time (*i*–*t*) chronoamperometric responses of N-rGO–CNT-0.2 and Pt/C at 0.78 V (*vs.* RHE). (d) The comparison of RDE polarization curves of N-rGO–CNT-0.2, Fe–N-rGO–CNT and Pt/C at a scan rate of 10 mV s^{-1} and a rotation speed of 1600 rpm. All data curves were recorded in 0.1 M O_2-saturated KOH.

be more active for ORR than pyrrolic N.[31–34] Taking into account the highest total nitrogen content achieved in N-rGO together while the best ORR performance was accomplished on N-rGO–CNT-0.2, the ORR activity of the N-rGO–CNT composite should not only depend on the amount and chemical state of active sites, but also be appreciably affected by mass transfer and electron transport. In the N-rGO–CNT-0.2 composite, the N-CNT part formed the 3D conductive network which enriched electrode–electrolyte–gas three-phase boundaries for sufficient mass transfer, and served as 'electron highways' for fast electron transport. The N-rGO part provided the high efficient catalytic sites for ORR. The close contact between N-rGO and N-CNT *via* strong pi–pi interaction would facilitate fast charge transport. As a balance of these facts, the best mass ratio of rGO and CNT was measured to be 1 : 5 in the present study.

In practical applications of fuel cells, fuel often goes across the exchange membrane from the anode to the cathode and deactivates the cathode catalyst. Therefore, the resistance to fuel crossover and durability should be tested for further evaluating an ORR catalyst.[36] In this study, LSV measurements were also carried out in the presence of 0.5 M methanol for both N-rGO–CNT-0.2 and commercial Johnson Matthey (JM) Pt/C (20 wt% Pt loading) catalysts to compare their tolerance to methanol crossover. As shown in Fig. 4a and b, the LSV curve of N-rGO–CNT-0.2 does not show any obvious shift in the presence of 0.5 M methanol while that of commercial Pt/C displays a significant negative shift (185 mV negative shift in half-wave potential), indicating that N-rGO–CNT-0.2 has excellent resistance to methanol crossover. On the other hand, the durability of the catalyst was also examined by chronoamperometric measurements in 0.1 M O_2-saturated KOH solution. Fig. 4c shows that the Pt/C catalyst suffers serious current descending while N-rGO–CNT-0.2 delivers much better durability.

Finally, in order to further explore the application of the present N-rGO–CNT composite, the improvement in its catalytic performance for ORR was demonstrated by introducing iron into the composite. It was interestingly found that the introduction of iron remarkably boosted the catalytic activity of the N-rGO–CNT composite. As shown in Fig. 4d, the on-set potential of Fe–N-rGO–CNT is comparable to that of the commercial Pt/C catalyst and the half-wave potential is only 41 mV negative than that of Pt/C. It was believed that this performance could be further enhanced by optimizing the preparation conditions of the catalysts.

Conclusion

In summary, nanocomposites of N-doped reduced graphene oxides and carbon nanotubes were prepared *via* a facile solution self-assembly route for exploring their application potential as ORR catalysts. It was interestingly found that the composition of nanocomposites significantly affected their ORR catalytic performance. The optimal mass ratio of rGO and CNT in N-rGO–CNT composites is 1 : 5. By incorporating the merits of the abundant highly-active sites from N-rGO and a 3D conductive network for efficient mass and electron transport from N-CNT, the N-rGO–CNT-0.2 composite exhibited a much enhanced ORR catalytic activity, excellent tolerance to methanol crossover and durability. Further improvement of the performance was also demonstrated by introducing iron into the composite. These results revealed the application potential of N-rGO–CNT as low-cost efficient electrocatalysts for ORR.

Acknowledgements

We gratefully thank the support from the National Key Project on Basic Research (Grant No. 2011CB808700, 2012CB215500, and 2012CB720300), the National Natural Science Foundation of China (Grant No. 91127044, and 21121063), and the Chinese Academy of Sciences.

Notes and references

1 I. Moussallem, J. Jorissen, U. Kunz, S. Pinnow and T. Turek, *J. Appl. Electrochem.*, 2008, **38**, 1177–1194.
2 M. Armand and J. M. Tarascon, *Nature*, 2008, **451**, 652–657.
3 G. Wu and P. Zelenay, *Acc. Chem. Res.*, 2013, **46**, 1878–1889.
4 M. K. Carpenter, T. E. Moylan, R. S. Kukreja, M. H. Atwan and M. M. Tessema, *J. Am. Chem. Soc.*, 2012, **134**, 8535–8542.
5 H. Tang, H. Yin, J. Wang, N. Yang, D. Wang and Z. Tang, *Angew. Chem., Int. Ed.*, 2013, **52**, 5585–5589.
6 H. Wang, Y. Liang, Y. Li and H. Dai, *Angew. Chem., Int. Ed.*, 2011, **50**, 10969–10972.
7 S. Guo, S. Zhang, L. Wu and S. Sun, *Angew. Chem., Int. Ed.*, 2012, **51**, 11770–11773.

8 Z. Cui, R. G. Burns and F. J. DiSalvo, *Chem. Mater.*, 2013, **25**, 3782–3784.
9 X. Sun, Y. Zhang, P. Song, J. Pan, L. Zhuang, W. Xu and W. Xing, *ACS Catal.*, 2013, **3**, 1726–1729.
10 J. Liang, Y. Jiao, M. Jaroniec and S. Z. Qiao, *Angew. Chem., Int. Ed.*, 2012, **51**, 11496–11500.
11 Q. Li, S. Zhang, L. Dai and L. S. Li, *J. Am. Chem. Soc.*, 2012, **134**, 18932–18935.
12 C. Zhang, N. Mahmood, H. Yin, F. Liu and Y. Hou, *Adv. Mater.*, 2013, **25**, 4932–4937.
13 G. Wu, K. L. More, C. M. Johnston and P. Zelenay, *Science*, 2011, **332**, 443–447.
14 M. Lefevre, E. Proietti, F. Jaouen and J. P. Dodelet, *Science*, 2009, **324**, 71–74.
15 Z. S. Wu, S. Yang, Y. Sun, K. Parvez, X. Feng and K. Mullen, *J. Am. Chem. Soc.*, 2012, **134**, 9082–9085.
16 R. J. Huo, W. J. Jiang, S. L. Xu, F. Z. Zhang and J. S. Hu, *Nanoscale*, 2014, **6**, 203–206.
17 Y. P. Xiao, W. J. Jiang, S. Wan, X. Zhang, J. S. Hu, Z. D. Wei and L. J. Wan, *J. Mater. Chem. A*, 2013, **1**, 7463–7468.
18 Z.-H. Sheng, L. Shao, J.-J. Chen, W.-J. Bao, F.-B. Wang and X.-H. Xia, *ACS Nano*, 2011, **5**, 4350–4358.
19 S. Wang, L. Zhang, Z. Xia, A. Roy, D. W. Chang, J.-B. Baek and L. Dai, *Angew. Chem., Int. Ed.*, 2012, **51**, 4209–4212.
20 C. H. Choi, S. H. Park and S. I. Woo, *ACS Nano*, 2012, **6**, 7084–7091.
21 Z. Yang, Z. Yao, G. Li, G. Fang, H. Nie, Z. Liu, X. Zhou, X. A. Chen and S. Huang, *ACS Nano*, 2011, **6**, 205–211.
22 V. C. Tung, L.-M. Chen, M. J. Allen, J. K. Wassei, K. Nelson, R. B. Kaner and Y. Yang, *Nano Lett.*, 2009, **9**, 1949–1955.
23 Y. Si and E. T. Samulski, *Chem. Mater.*, 2008, **20**, 6792–6797.
24 P. Chen, T.-Y. Xiao, Y.-H. Qian, S.-S. Li and S.-H. Yu, *Adv. Mater.*, 2013, **25**, 3192–3196.
25 A. M. Cao, J. S. Hu and L. J. Wan, *Sci. China: Chem.*, 2012, **55**, 2249–2256.
26 T.-K. Hong, D. W. Lee, H. J. Choi, H. S. Shin and B.-S. Kim, *ACS Nano*, 2010, **4**, 3861–3868.
27 L. Qiu, X. Yang, X. Gou, W. Yang, Z.-F. Ma, G. G. Wallace and D. Li, *Chem. – Eur. J.*, 2010, **16**, 10653–10658.
28 P. Han, Y. Yue, Z. Liu, W. Xu, L. Zhang, H. Xu, S. Dong and G. Cui, *Energy Environ. Sci.*, 2011, **4**, 4710–4717.
29 F. Tristán-López, A. Morelos-Gómez, S. M. Vega-Díaz, M. L. García-Betancourt, N. Perea-López, A. L. Elías, H. Muramatsu, R. Cruz-Silva, S. Tsuruoka, Y. A. Kim, T. Hayahsi, K. Kaneko, M. Endo and M. Terrones, *ACS Nano*, 2013, **7**, 10788–10798.
30 Z. Jin, H. Nie, Z. Yang, J. Zhang, Z. Liu, X. Xu and S. Huang, *Nanoscale*, 2012, **4**, 6455–6460.
31 R. Silva, D. Voiry, M. Chhowalla and T. Asefa, *J. Am. Chem. Soc.*, 2013, **135**, 7823–7826.
32 L. Lai, J. R. Potts, D. Zhan, L. Wang, C. K. Poh, C. Tang, H. Gong, Z. Shen, J. Lin and R. S. Ruoff, *Energy Environ. Sci.*, 2012, **5**, 7936–7942.
33 T. Sharifi, G. Hu, X. Jia and T. Wågberg, *ACS Nano*, 2012, **6**, 8904–8912.
34 K. Ai, Y. Liu, C. Ruan, L. Lu and G. Lu, *Adv. Mater.*, 2013, **25**, 998–1003.
35 W. Ding, Z. D. Wei, S. G. Chen, X. Q. Qi, T. Yang, J. S. Hu, D. Wang, L. J. Wan, S. F. Alvi and L. Li, *Angew. Chem., Int. Ed.*, 2013, **52**, 11755–11759.
36 Y. Tan, C. Xu, G. Chen, X. Fang, N. Zheng and Q. Xie, *Adv. Funct. Mater.*, 2012, **22**, 4584–4591.